AIChE
JOURNAL

Flow, suspension, and mixing dynamics in DASGIP bioreactors: Part 1

Jasmin J. Samaras[1] ⓘ | Martina Micheletti[1] ⓘ | Andrea Ducci[2] ⓘ

[1]Department of Biochemical Engineering, University College London, London, UK

[2]Department of Mechanical Engineering, University College London, London, UK

Correspondence
Andrea Ducci, Department of Mechanical Engineering, University College London, Torrington Place, London WC1E 7JE, UK.
Email: a.ducci@ucl.ac.uk

Abstract

The bioreactor flow environment has a significant impact on process performance, especially in stem cell cultures. The work of Correia et al found intermittent agitation modes to improve induced pluripotent stem cell (iPSC)-cardiomyocyte differentiation yields; however, to date, the impact within the flow has not been fully characterized. This work aims to characterize the flow dynamics occurring within a commercially available DASGIP bioreactor, equipped with a two-blade paddle impeller, operating under different agitation modes and for two bottom geometries. The paddle impeller configuration generated an axial flow profile due to a large impeller D/T and blade confinement with the bioreactor wall. The application of intermittent agitation was shown to induce two transient spikes in flow velocity and shear stress, the amplification of which increased with dwell duration. Marginally increasing the dwell duration was shown previously to increase differentiation yields, therefore it can be stipulated that introduction of these spikes was favorable toward cardiogenic differentiation.

KEYWORDS
agitation modes, bioreactor geometry, DASGIP, flow dynamics, PIV

1 | INTRODUCTION

Characterization of the flow dynamics in stirred tanks of standard geometry is well documented in the literature. However, for process development studies, it is more common to encounter commercially available bioreactors with nonstandard configurations.[1,2] As an example, the CellReady Mobius (Applikon) single use reactor, commonly used in cell culture,[3] comprises a torispherical bottom geometry, equipped with an up-pumping marine impeller (D/T = 0.54, C/T = 0.18). In comparison, the BioBLU (Eppendorf) single use reactor, which is also recommended for cell culture applications,[4] has a flat bottom geometry and is equipped with one or two downpumping pitched blade turbine impellers (D/T = 0.42, C/T = 0.25).[5] The DASGIP bioreactors (Eppendorf) are another example,[6] available with both flat and round bottom configurations and equipped with either a pitched blade turbine impeller (D/T = 0.48) or a two-blade paddle impeller of large impeller to tank diameter ratio (D/T = 0.97).

Factors such as the impeller design, that is, axial or radial flow types, off-bottom clearance, blade diameter, pitch and thickness, and vessel configuration, that is, geometry, baffled or unbaffled, round or flat bottom, have all been demonstrated to influence the mean flow, turbulence levels and the trailing vortices generated at the back of the blade.[7,8] Distinct mean flow circulation patterns and blade trailing vortices are created from different impeller types. These are responsible for enhancing mixing and controlling mass transfer.[9] Radial Rushton turbine impellers develop a pair of trailing vortices behind the upper and lower edges of the blade, characterized by mean radial velocities up to $0.62–0.87V_{tip}$.[10-12] Both vortices extend radially toward the

reactor wall with the upper vortex exhibiting a slight inclination when D/T and C/T = 0.33.[13-15] Axial pitched blade turbine impellers generate a single and inclined trailing vortex behind each turbine blade with axial velocities up to 0.45–0.55V_{tip}.[16-18] Minimal radial displacement and downward/upward axial displacement is exhibited, depending upon whether agitation is in down- or up-pumping mode.[18]

Of particular interest in this work is the impact of the impeller to tank diameter ratio, D/T, upon the flow, in addition to the difference between baffled and unbaffled bioreactor configurations. The study of Ramsay et al[19] characterized the flow field of a "butterfly" impeller for D/T = 0.53–0.98. It was found that as D/T increased, ensemble-averaged velocity magnitudes discharged by the impeller decreased by approximately 40%. Similarly, Hall et al[20] found that eccentrically agitated vessels equipped with pitched blade turbine impellers exhibited a similar reduction in velocity magnitudes on the side where the impeller discharge stream is confined by the bioreactor wall.[20] Both studies found that increasing confinement at the bioreactor wall, either from impeller eccentricity or from large impeller to tank diameter ratio D/T, results in a reduction of velocity magnitudes. The study of Hall et al[20] also found a reduction in velocity magnitudes between unbaffled and baffled vessel configurations. In general, independently of the impeller type employed, Hall et al[20,21] and Montante et al[22] found that unbaffled configurations are mainly characterized by solid body rotation with the tangential velocity component being the most intense and presenting significantly diminished flow circulation patterns in the axial and radial direction in comparison to their baffled counterparts. Tamburini et al[23] used CFD methods to predict the flow field in both baffled and unbaffled vessels, equipped with a Rushton turbine impeller. They found that for fully turbulent flow conditions, the radial and tangential components within the baffled vessel were reduced and converted into axial flow. In the unbaffled configuration solid body rotation occurred and a lower level of turbulence was achieved. Other studies also reported this effect.[24,25]

In addition to the physical configuration of a bioreactor, the rotational speed and agitation strategy greatly affect cell behavior, the flow, mixing, and suspension dynamics. Ismadi et al[26] investigated the flow dynamics in spinner flasks to assess the impact of agitation upon iPSC proliferation using microcarrier technology. The maximal local shear was shown to increase linearly with rotational speed and optimal cell proliferation was achieved at N = 25 rpm, with shear stress levels up to 0.0984 Pa. With a further increase in speed, at N = 28 rpm, microcarrier attachment was no longer maintained and a reduction in iPSC proliferation was realized with only a marginal 10% increase in maximum shear stress (0.108 Pa). Such significant contrasting effects within a small shear stress and rotational speed range demonstrate how susceptible stem cells are to their hydrodynamic environment and how relevant it is to characterize the flow dynamics of commercially available stirred bioreactors.

Wang et al[27] also observed that hydrodynamic shear reduces differentiation efficiency in stem cell cultures under continuous agitation and hypothesized that this reduction could be alleviated through intermittent agitation regimes. Previously published works have also demonstrated the beneficial impact of designing stem cell differentiation protocols that introduce a mechanical stimulus through pulsatile flow or intermittent agitation.[1,28-30] For example, Correia et al[1] found a fourfold increase in iPSC-cardiomyocyte differentiation yields when operating under intermittent agitation modes in comparison to continuous agitation. These findings were further corroborated by the study of Samaras et al[2] who found that optimization of the dwell time, that is, the time duration the impeller is stationary during intermittent agitation, led to a further 66% increase in differentiation yields.[2] Both these works were carried out in a DASGIP reactor. Intermittent agitation strategies may also be recommended in 3D cell culture to improve microcarrier adherence protocols during the initial period post-inoculation.[31-34] Overall, the impact of intermittent agitation upon cardiogenic differentiation procedures and during cell culture has been proven to be beneficial; however, only the study of Samaras et al[35] can be found in the literature addressing the mixing and suspension dynamics for intermittent agitation mode in a commercial bioreactor, and more studies are needed providing a full flow characterization for a variable impeller speed strategy. The present work builds upon the studies of Correia et al[1] and Samaras et al[2,35] and aims at providing an in-depth investigation of the flow dynamics occurring in a nonstandard, commercially available DASGIP bioreactor with two different bottom geometries, focusing upon characterizing circulation patterns, trailing vortices, shear stresses, and vorticity levels, obtained under continuous and intermittent agitation modes. This flow characterization is essential to lay the foundations for a better understanding of stem cell differentiation processes and identify novel agitation strategies for optimal process control and performance.

2 | MATERIALS AND METHODS

2.1 | Bioreactor configurations

A flat- and a round-bottomed DASGIP Cellferm-pro bioreactor systems (Eppendorf, Germany), with heights, H = 15.5 and 16.5 cm and internal diameter, T = 6.2 cm, were equipped with a 6 cm diameter trapezoidal paddle impeller at an off-bottom clearance, C = 1 cm (D/T = 0.97, C/H_L = 0.15) and C = 1.95 cm (D/T = 0.97, C/H_L = 0.26). A schematic of each bioreactor configuration is given in Figure 1a. A working volume of V_w = 0.20 L MilliQ water was used in both bioreactor configurations, corresponding to liquid heights, H_L = 6.62 and 7.4 cm. For the engineering characterization, modifications were made to the original magnetically driven bioreactor to achieve motor-driven agitation. The impeller shaft was extended and attached to an N-Series Allen Bradley Motor unit. To minimize optical distortion due to the curvature of the vessel the system was mounted within a water filled glass trough, shown in Figure 1b.

2.2 | Particle image velocimetry and data processing

A green diode laser, with an output power rating of 300 mW and wavelength, λ = 532 nm, was used for the two-dimensional
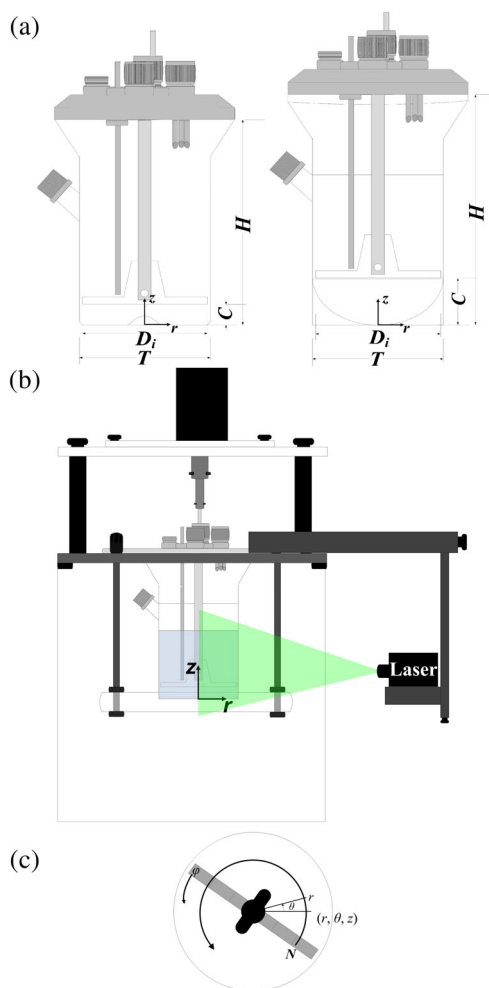
FIGURE 1 (a) Schematic diagram of the flat- (left) and round-(right) bottom geometry bioreactors, (b) experimental setup, and (c) bioreactor horizontal cross-section with reference system [Color figure can be viewed at wileyonlinelibrary.com]

(2D) particle image velocimetry experiments, together with a cylindrical lens, a high resolution ($1,260 \times 1,024$) intensified NanoSense MKII camera (Dantec Dynamics A/S, Denmark) and a timing box. A 1 mm vertical laser sheet was produced, intersecting the shaft and illuminating half of the bioreactor midsection to measure the radial and axial velocity components. A schematic diagram of the setup is provided in Figure 1b. Rhodamine-coated polymethyl methacrylate spheres, $20–50 \mu m$ (Dantec Dynamics A/S), were used to seed the flow, while the camera was equipped with a 570 nm orange light cut-off filter to minimize laser light reflection at the wall and optimize seeding particles detection.

The cylindrical coordinate reference system (r, θ, z) shown in Figure 1c was employed, where the origin is positioned at the center of the reactor base and anticlockwise impeller rotation, when the system is seen from above, is considered positive. It should be noted that in some of the results reported in this work, reference is made to negative radial coordinates, r, which, although not consistent with the cylindrical coordinate system employed, are used to discriminate

between the left and right side of the reactor about the impeller axis. The origin of the phase angular coordinate, φ, is set on the leading blade of the impeller, $\varphi = 0°$.

The maximum local shear rate, γ_{max}, in the vertical plane was obtained from the principal components of the strain rate tensor.[36,37]

In continuous agitation modes, phase-resolved measurements were synchronized with the impeller position using the servo motor encoder. The impeller encoder signal is given to a timing box which synchronizes the camera trigger with the desired impeller position. This was done through IDT software, where a time delay can be selected for instantaneous vector maps corresponding to the desired angular position from the leading impeller blade. Twelve phase angles were investigated for each continuous agitation condition, between $\varphi = 0–165°$, in increments of $15°$. Five hundred image pairs were obtained for each measurement condition, with a time delay between images in each pair of 3.5, 3, 2.5, and 2 ms for continuous rotational speeds of 75, 90, 105, and 120 rpm, respectively ($\approx 1.5°$ of impeller rotation). The time interval was selected such as to minimize the number and magnitude of erroneous vectors and/or "outliers" generated from the adaptive correlation analysis. This was applied in two passes with an initial interrogation window of 32×32 pixels and a final window size of 16×16 pixels. With a 50% interrogation area overlap, this resulted in a final resolution of 8×8 pixels, corresponding to a final measurement spatial resolution of $\Delta r = \Delta z = 0.12$ mm.

The flat-bottomed DASGIP bioreactor was also used for investigation of intermittent agitation profiles. In this case, three time components are defined, namely the impeller rotational speed, N, the interval time, T_{inv}, and the dwell/stop time, T_{dwell}. T_{inv} is the time during which the impeller is in motion and T_{dwell} defines how long the impeller is stopped. Intermittent agitation experiments were carried out for $N = 90$ rpm, $T_{inv} = 30$ s and $T_{dwell} = 500–30,000$ ms. Two different sets of measurements were obtained during either impeller motion (T_{inv}) or dwell (T_{dwell}) phases. Measurements taken during impeller motion were obtained for every revolution at $\varphi = 0°$ (i.e., blade aligned with the vertical measurement plane). This measurement was repeated over 10 consecutive intervals. To capture the flow transient when the impeller was stopped, measurements during the impeller dwell phase were obtained in a time-resolved manner with an acquisition frequency rate of 0.02 kHz. Averages at different corresponding times after the impeller stoppage were carried out over 10 consecutive dwell phases. Images were then processed using a purposely-written MATLAB program.

3 | RESULTS AND DISCUSSION

The following section is divided into four parts; Sections 3.1 and 3.2 explore the ensemble-averaged and phase-averaged flow characteristics of the flat and round bottom DASGIP configurations, respectively, under continuous agitation modes. Section 3.3 presents an in-depth characterization of the trailing vortices in both bioreactor configurations, followed in Section 3.4 by the characterization of the flow dynamics during intermittent agitation.

3.1 | Ensemble-averaged flow measurements—Continuous agitation

The first part of this study aimed at characterizing the flow field for two DASGIP bioreactor configurations operating under continuous agitation. This was performed to determine the flow variation due to the different bottom geometries. 2D contour maps of the ensemble-averaged velocity magnitude based on the radial and axial components, $\overline{U_{rz}}/V_{tip}$, and the ensemble-averaged root mean square (r.m.s) of the axial, $\overline{U'_z}/V_{tip}$ and radial, $\overline{U'_r}/V_{tip}$, velocity components are presented in Figure 2a–c, superimposed with the corresponding velocity vector fields for $N = 90$ rpm ($Re = 5,400$). To better compare the flow fields of the two reactors, each figure shows the flat and round bottom bioreactor configurations on the left and right halves of the plot, with the impeller centerline aligned between the two. It should be noted that in both cases the impeller blade is moving toward the reader (i.e., anticlockwise on the left side and clockwise on the right). Results are reported for one reference speed, $N = 90$ rpm, as it was found that the velocity fields scaled relatively well with V_{tip}, both in terms of magnitude ($\overline{U_{rz}} = 0$–$0.1 \ V_{tip}$) and velocity direction, considering rotational speeds in the range, $N = 75$–120 rpm ($Re = 4,500$–$7,200$). Generally, the nondimensional velocity magnitudes in Figure 2a were observed to decrease by 8.5 and 5% in the flat and round bottom configurations, respectively, with increasing rotational speed. This behavior is related to the narrow gap between the impeller tip and the bioreactor wall, which prevents radial flow development. This effect becomes more pronounced for greater rotational speeds. Consequently, the impeller discharge zone shows reduced radial flow due to the large D/T, with the bioreactor wall splitting and redirecting the impeller jet into two axial streams. This is more evident in the flat bottom reactor, where the radial jet instantly impinges on the bioreactor wall at a vertical position of $z/H_L \approx 0.26$, leading to the formation of two counterrotating circulation zones of equal intensity, above and below the impeller region. This is less pronounced in the round bottom reactor, where there is a clear imbalance between the two circulation loops, with the upper loop being denoted by velocity intensities two times greater than the lower loop. The top circulation loops in both configurations reach a height of approximately $z/H_L \approx 0.9$. Comparison of the upper circulation region across the two bioreactor configurations shows the round bottom is characterized by velocities greater than the corresponding circulation zone of the flat bottom (approximately 24% increase in velocity magnitude). This suggests the round configuration is more effective at creating a homogeneous environment for cells over the entire bioreactor volume. Conversely, the circulation loop present below the impeller in the flat bottom reactor, characterized by velocity magnitudes 20% higher, suggests more efficient lift of cells from the bioreactor base.

The ensemble-averaged r.m.s for each velocity component accounts for both the pseudo-turbulence due to the periodic fluctuations induced by blade passage, and the random fluctuations due to the local presence of turbulence. The contour maps in Figure 2b,c are shown for one reference rotational speed, $N = 90$ rpm, as it was again found to scale well for increasing impeller tip speed. This suggests that
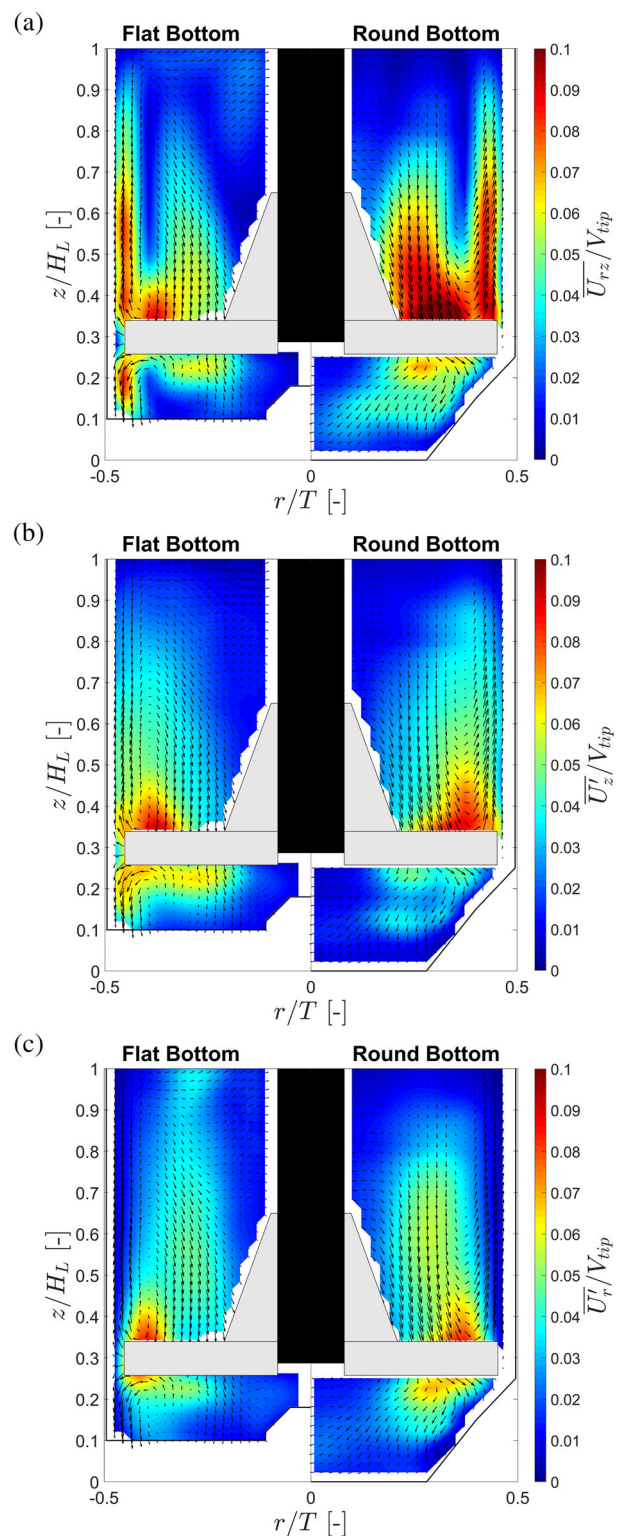

FIGURE 2 Contour maps of ensemble-averaged flow characteristics at $N = 90$ rpm for both bioreactor configurations: (a) velocity magnitude, U_{rz}; (b) axial r.m.s velocity, U'_z; and (c) radial r.m.s velocity, U'_r [Color figure can be viewed at wileyonlinelibrary.com]

the mean flow is fully developed and exhibits a turbulent regime in the range of rotational speeds investigated. Radial and axial velocity fluctuations determined in this work ranged between 0 and $0.1V_{tip}$.

These are comparable to r.m.s values usually encountered with axial flow impellers ($\overline{U'_z}$ = 0.1–0.15V_{tip} and $\overline{U'_r}$ = 0.1–0.15V_{tip}),[18,38-40] while they are significantly higher with radial flow impellers ($\overline{U'_z}$ and $\overline{U'_r}$ ≈ 0.32V_{tip}).[41] From Figure 2b,c, the r.m.s velocities are greatest in the impeller region, where the trailing vortices are formed, and reach up to 0.098 V_{tip} for the flat configuration and 0.110 V_{tip} for the round. It is also worth noting that the maximum r.m.s values are comparable in magnitude to the ensemble-averaged axial velocities and are in fact three times larger than the ensemble-averaged radial velocities, indicating large velocity fluctuations (random and periodic) in the impeller region.

A quantitative comparison of the axial circulation loops, emanating from and returning to the impeller region, can be obtained from Figure 3. Radial profiles of the ensemble-averaged axial velocity component are shown at three elevations, indicated in the inset. As mentioned above it is immediately evident that the velocities scale well with the impeller tip velocity for both bioreactor configurations at the range of impeller rotational speeds investigated. The axial velocity profile for the bulk flow was taken at z/H_L = 0.775 and shows positive axial velocities close to the bioreactor wall, indicating upward flow, which then decreases as radial positions closer to the tank axis are considered, with negative axial velocities at r/T ≈ 0.3, corresponding to the downward flow of the upper circulation loop. This then plateaus to $\overline{U_z}$ ≈ 0V_{tip} toward the impeller axis. Comparison between the two bioreactor configurations shows similar axial velocity profiles, although the negative velocity region, associated to the returning stream of the upper loop, is limited to a lower range of radial distances, r/T = 0.2–0.4 in the flat bottom when compared to the round bottom, r/T = 0.15–0.38. In general, it can be concluded that at this height both circulation loops for the flat and round bottom configurations have similar velocity intensities, while a slightly wider

recirculation loop is present in the round bottom configuration. The second elevation considered is above the impeller at z/H_L = 0.388. The profiles for the two bioreactor configurations are similar, but as previously mentioned, the round bottom bioreactor exhibits a wider recirculation loop, in addition to greater positive and negative axial velocities. This indicates a stronger upper recirculation loop in comparison to the flat bottom bioreactor in proximity of the impeller. The lowest elevation profile was obtained below the impeller at z/H_L = 0.182. Two distinct radial profiles of the axial velocity are now observed between the bioreactor configurations: the round bottom system shows weak downward flow with the apparent absence of a prominent lower circulation loop. Negative axial velocities are observed close to the bioreactor wall in the flat bottom configuration, which then increase to positive values at r/T ≈ 0.4 as radial coordinates closer to the impeller axis are considered. In agreement with Figure 2, this indicates the presence of a lower circulation loop.

3.2 | Phase-resolved flow measurements—continuous agitation

2D phase-resolved contour maps of the in-plane velocity magnitude, $\langle U_{rz} \rangle / V_{tip}$, superimposed with the corresponding velocity vector fields, are given in Figure 4 for φ = 0, 30, 45, and 60° at N = 90 rpm in the flat bottom configuration. In Figure 4, data are only shown for φ = 0–60° because the velocity field exhibited the greatest variation in this range of phase angles. As the impeller rotates, the velocity magnitudes are shown to increase in intensity, corresponding to the trailing vortex formation behind the blade. The most intense velocity magnitudes are confined to the impeller region, in proximity of the upper and lower trailing vortices and along the bioreactor wall after
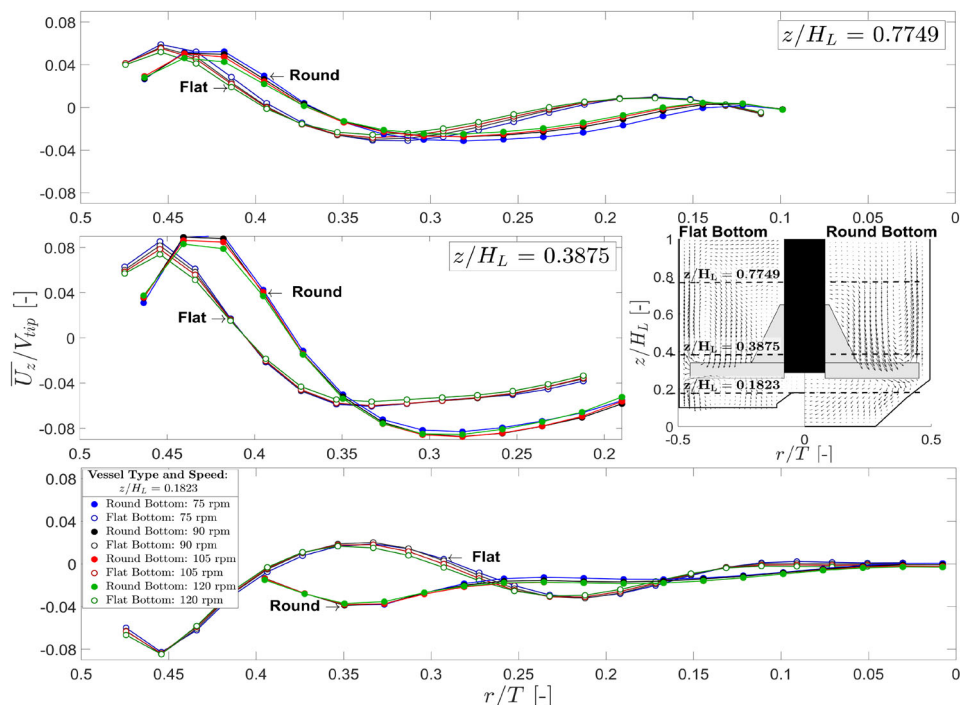

FIGURE 3 Comparison of ensemble-averaged axial velocity profiles for the flat and round bottom bioreactors at three elevations, z/H_L = 0.775, 0.388, and 0.182 with increasing rotational speeds [Color figure can be viewed at wileyonlinelibrary.com]
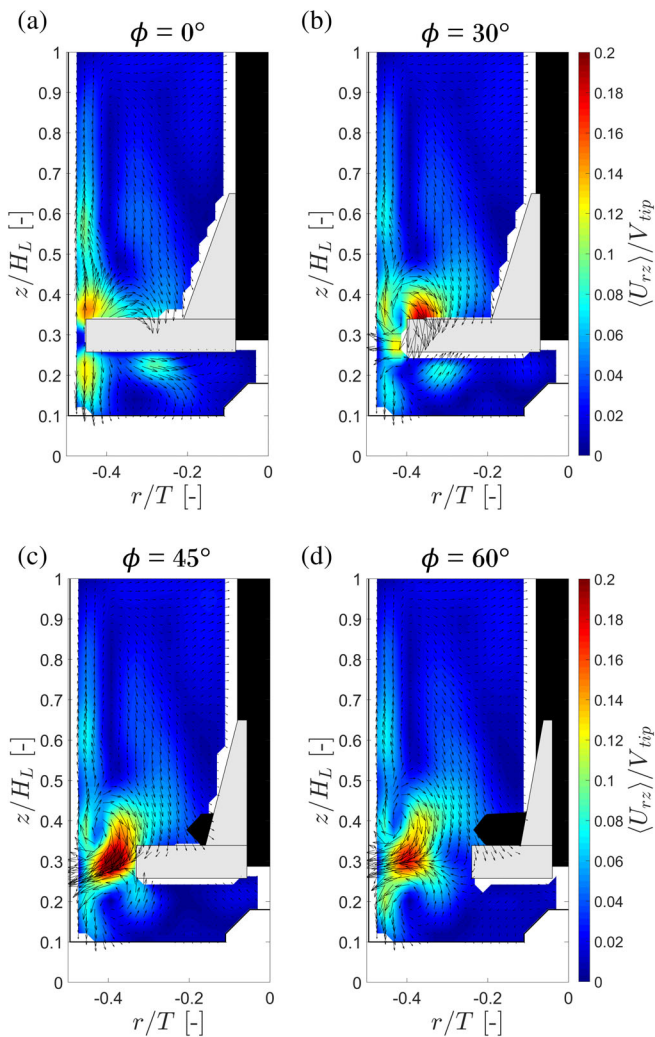
FIGURE 4 Contour maps of phase-resolved velocity magnitude at N = 90 rpm for the flat bottom bioreactor configuration: (a) φ = 0°, (b) φ = 30°, (c) φ = 45°, (d) φ = 60° [Color figure can be viewed at wileyonlinelibrary.com]

FIGURE 5 Contour maps of phase-resolved velocity magnitude at N = 90 rpm for the round bottom bioreactor configuration: (a) φ = 0°, (b) φ = 30°, (c) φ = 45°, and (d) φ = 60° [Color figure can be viewed at wileyonlinelibrary.com]

the impinging radial jet splits into two vertical streams. With impeller blade rotation from φ = 0–45°, there is a general increase in velocity magnitude intensity and the top trailing vortex appears to dominate the flow. As the impeller continues to rotate, the velocity magnitudes are shown to decrease with increasing measurement plane distance from the impeller blade and the two vortices are shown to display similar intensities in their outer velocity. It is worth noting that the highest reached velocity magnitude of $\langle U_{rz}\rangle/V_{tip}$ = 0.22–0.23 at φ = 45° is approximately 145% higher than the ensemble-averaged results (see Figure 2a). The stream emanating from the impeller is nearly radial up to an angle of 30°, before it starts to be deflected downward due to the imbalance between the upper and lower trailing vortices (φ = 45 and 60°).

Figure 5 displays the phase-resolved contour maps for φ = 0, 30, 45, and 60° for the round bottom configuration at N = 90 rpm. Unlike the flat bottom configuration, the upper vortex alone dominates the bioreactor flow over the entire cross-section. From this point of view,
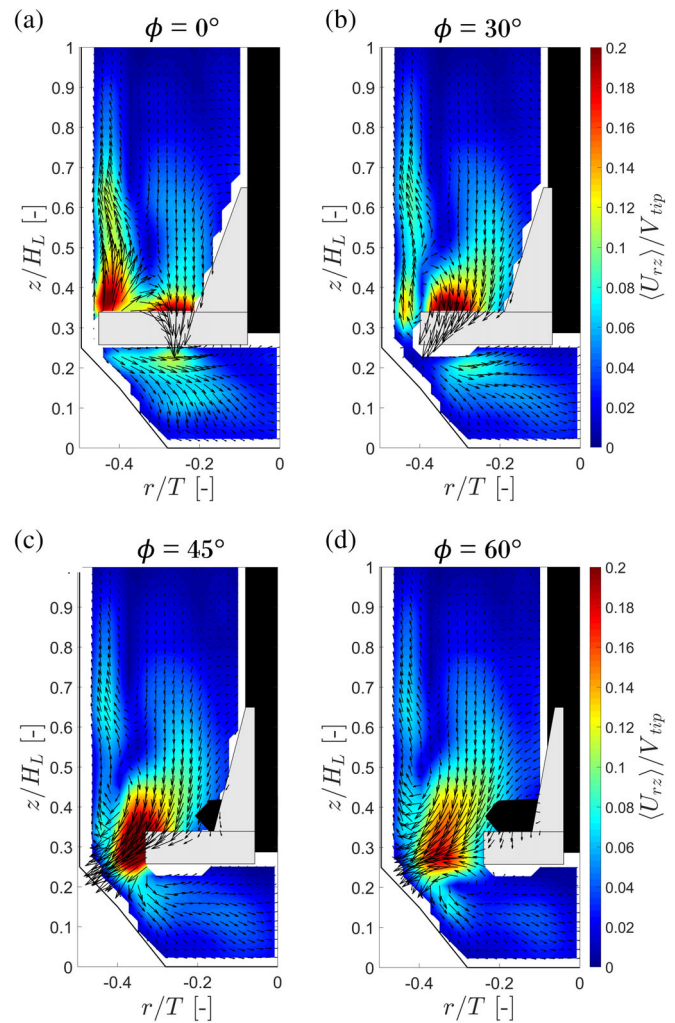
the area characterized by velocities magnitude, $\langle U_{rz}\rangle \geq 0.12V_{tip}$ is observed to increase by 59–77% over the phase angles considered when compared against the corresponding area for a flat configuration.

Figure 6 presents the phase-resolved axial velocity component at three individual points for all rotational speeds investigated (N = 75–120 rpm) in both bioreactor configurations. The plot of a full rotation was obtained by stacking back-to-back 180° phase-resolved data. The three points were observed in the upper region of the bioreactor, in the impeller region and below the impeller, z/H_L = 0.61, 0.36, and 0.18, and r/T = 0.45, 0.45, and 0.45 (flat) or 0.35 (round), respectively. The points selected were close to the bioreactor walls to observe the edges of the circulation zones in both configurations, as indicated in the inset of Figure 6. Generally, the superimposed lines show good scaling at the rotational speeds investigated when normalized against V_{tip} and close similarity between the two configurations. The upper-most point (z/H_L = 0.61, r/T = 0.45) shows weak positive axial
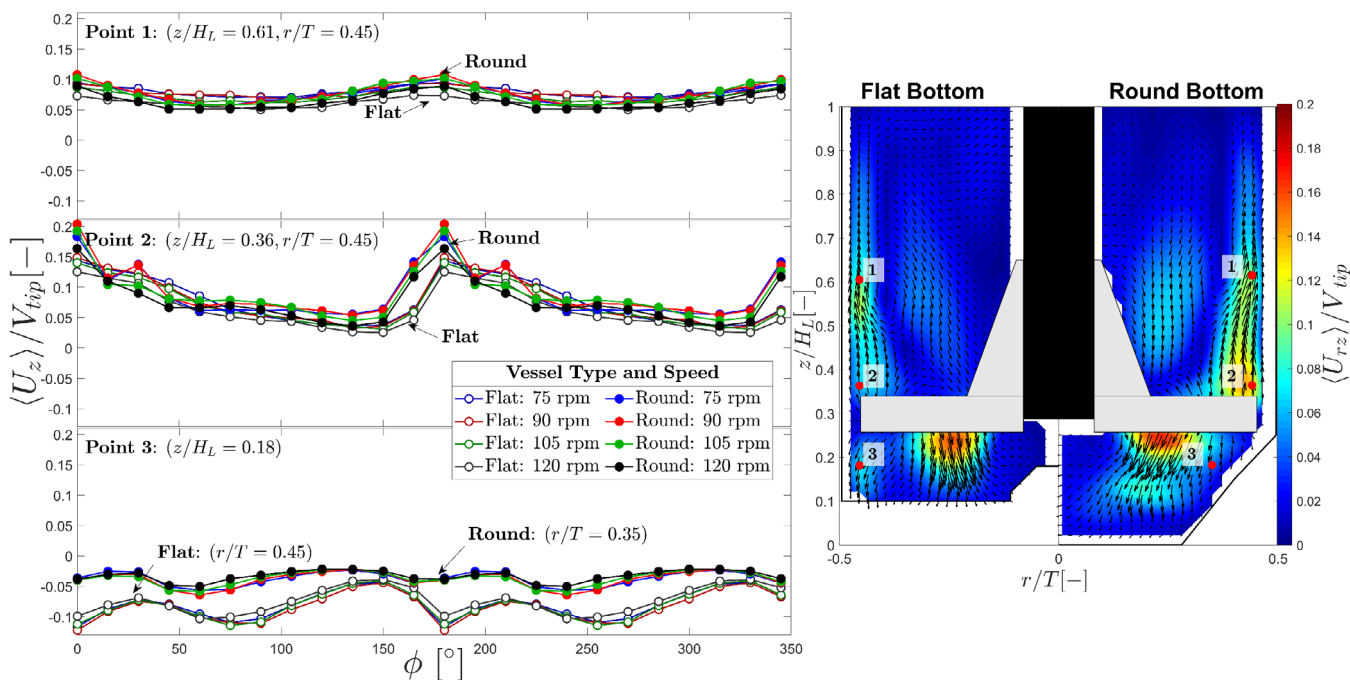
FIGURE 6 Comparison of phase-resolved axial velocity for the flat and round bottom bioreactors at three single points with increasing rotational speeds over an impeller revolution [Color figure can be viewed at wileyonlinelibrary.com]

FIGURE 7 Comparison of phase-resolved radial velocity for the flat and round bottom bioreactors at three single points with increasing rotational speeds over an impeller revolution [Color figure can be viewed at wileyonlinelibrary.com]
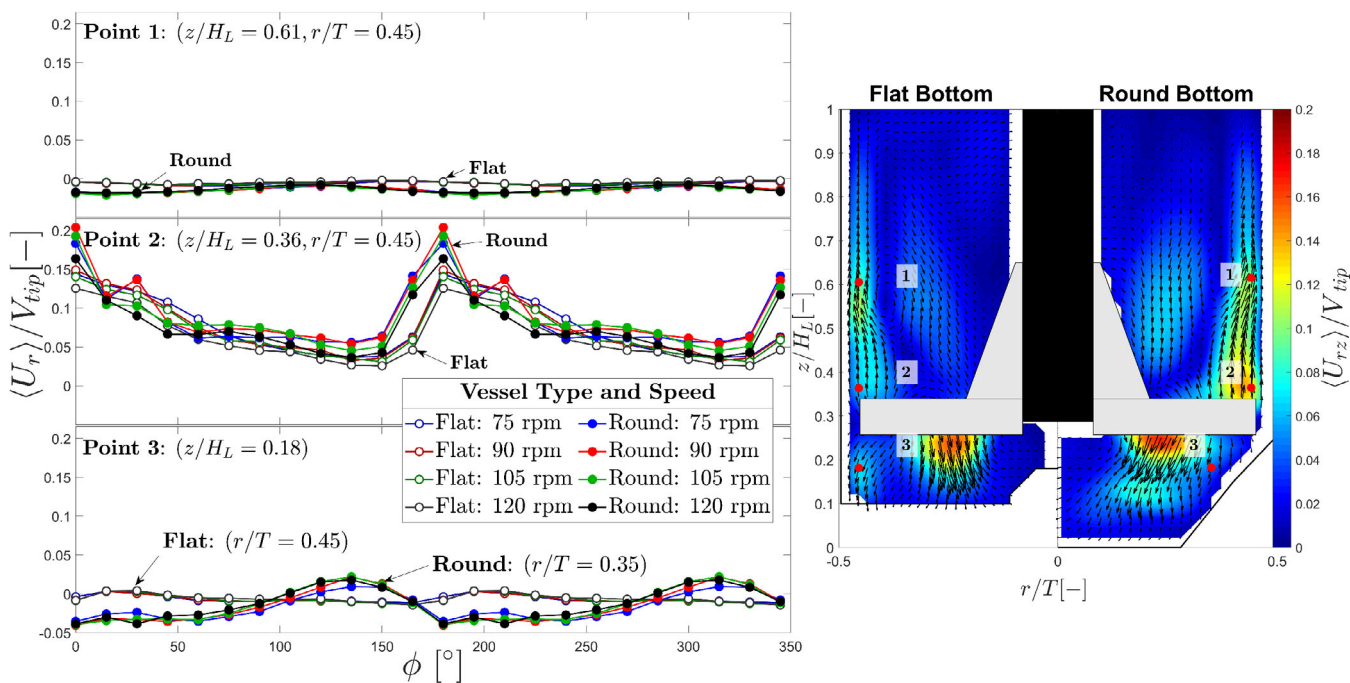
velocities with little change as the impeller rotates. There is a subtle increase in the axial velocities as the impeller rotates past the plane of measurement which then decreases as the distance between the impeller tip and the plane of measurement increases. Observing point 2, within the impeller region, the same trend is apparent; however,

the axial velocities increase up to $0.2V_{tip}$ (round) and $0.15V_{tip}$ (flat) as the impeller passes the plane of measurement at low-phase angles and drops to $0.05V_{tip}$ as this distance increases. The decrease in axial velocities in the impeller blade's wake corresponds to the decay in intensity of the two trailing vortices. Good scaling can again be

observed, however, the axial velocities do not reach as high an intensity within the flat bottom configuration. This suggests a more intense upper circulation loop occurring within the round bottom configuration. Below the impeller, the opposite effect is apparent. As before, there is little distinction of changing axial velocities during impeller blade passage. Negative axial velocities ($\approx -0.05V_{tip}$) indicate a generally downward flow direction away from the impeller toward the bioreactor base and good scaling is again apparent. In the flat bottom configuration, more intense negative axial velocities are representative of the lower trailing vortex, mostly observed at low-phase angles when the impeller is in proximity of the measurement plane.

The same three-point analysis was performed, considering the radial velocity components in both bioreactor configurations for $\varphi = 0$–$345°$. This is shown in Figure 7. Point 1 ($z/H_L = 0.61$, $r/T = 0.45$) in the upper region close to the reactor wall shows almost no radial flow in both bioreactor configurations. However, the radial flow within the impeller region at Point 2 gives a greater contribution to the local flow dynamics. Similar to the axial flow, at low-phase angles radial velocities increase up to $0.2V_{tip}$ (round) and $0.15V_{tip}$ (flat). A positive radial displacement toward the bioreactor walls is detected when the blade is in the impeller region, decreasing close to zero ($\approx 0.03V_{tip}$) after the impeller blade passage at $\varphi = 45$–$165°$. Similar to the previous results, good scaling is evident for both configurations and the round configuration displays a more intense upper circulation loop. When Point 3 below the impeller is considered, weak negative radial velocities within the round bottom configuration represent inward flow toward the impeller shaft at low-phase angle. This then increases to 0 at $\varphi = 105$–$150°$ with the decay of the lower circulation loop as impeller blade passage continues until the second blade approaches the plane. The flat bottom configuration shows little/no radial flow below the impeller at the point considered.

3.3 | Trailing vortices characterization—continuous agitation

To visualize the trailing vortices generated in the impeller wake, 2D phase-resolved contour maps of the vorticity are vertically stacked for 24 phase angles, $\varphi = 0$–$345°$, at $N = 90$ rpm in Figure 8a,b for the flat and round bottom configurations, respectively. A high inclination of the upper vortex is observed in both configurations, moving upwards from $z/H_L \approx 0.3$ to $z/H_L \approx 0.7$ in the flat (a) and $z/H_L \approx 0.8$ in the round (b). The vortex intensity is highest at $\varphi = 30°$ and decays by approximately 65 and 63% at a phase angle $\varphi = 165°$ for the flat and round bottom configurations, respectively. The lower vortex is identifiable in the flat bottom reactor for almost the full impeller rotation, decaying by approximately 78% at $\varphi = 150°$. Conversely, up to 95% decay in the lower vortex intensity is measured in the round bottom reactor, showing a transient vortex with much more rapid decay behind the leading blade.

A 3D visualization of the trailing vortices generated behind the blade over a full rotation is shown in Figure 8c at $N = 90$ rpm, where the trailing vortices were identified from iso-vorticity surfaces
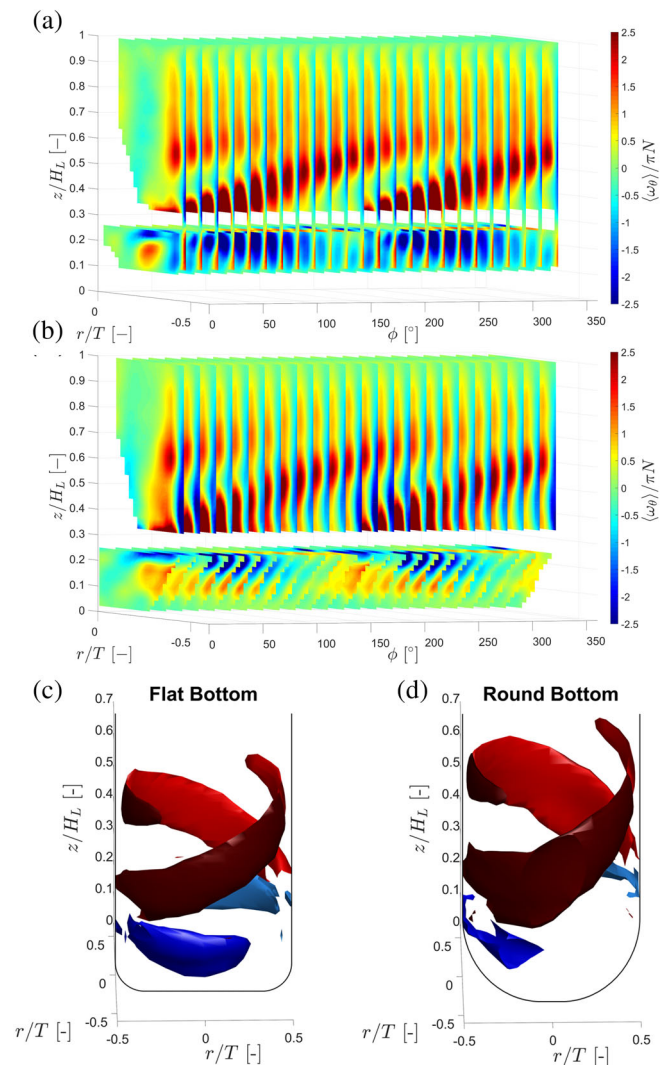

FIGURE 8 Trailing vortices characterization: (a) staggered contour maps of the phase-resolved vorticity for increasing φ for the flat bottom configuration, $N = 90$ rpm; (b) staggered contour maps of the phase-resolved vorticity for increasing φ for the round bottom configuration, $N = 90$ rpm; (–c,d) 3D visualization of the trailing vortices for the flat (c) and round (d) bottom bioreactors at $N = 90$ rpm [Color figure can be viewed at wileyonlinelibrary.com]

($|\langle\omega_\theta\rangle/\pi N| = 1.5$). The two vortices are clearly separated above and below the impeller blade and as expected, the upper vortices are shown to curve upward, extending axially behind the blades. The lower trailing vortex is clearly discernible for the flat configuration, while its structure for the round configuration is less captured by the iso-vorticity threshold selected. To observe axial and radial evolution of the two trailing vortices, the axial and radial coordinates of the center of each trailing vortex was calculated using Equation (1):

$$X_g = \frac{\sum \omega_i \times X_i}{\sum \omega_i} \tag{1}$$

where ω_i and X_i are the vorticity and axial or radial coordinates of any point within the stated iso-vorticity boundaries. Figure 9 shows the
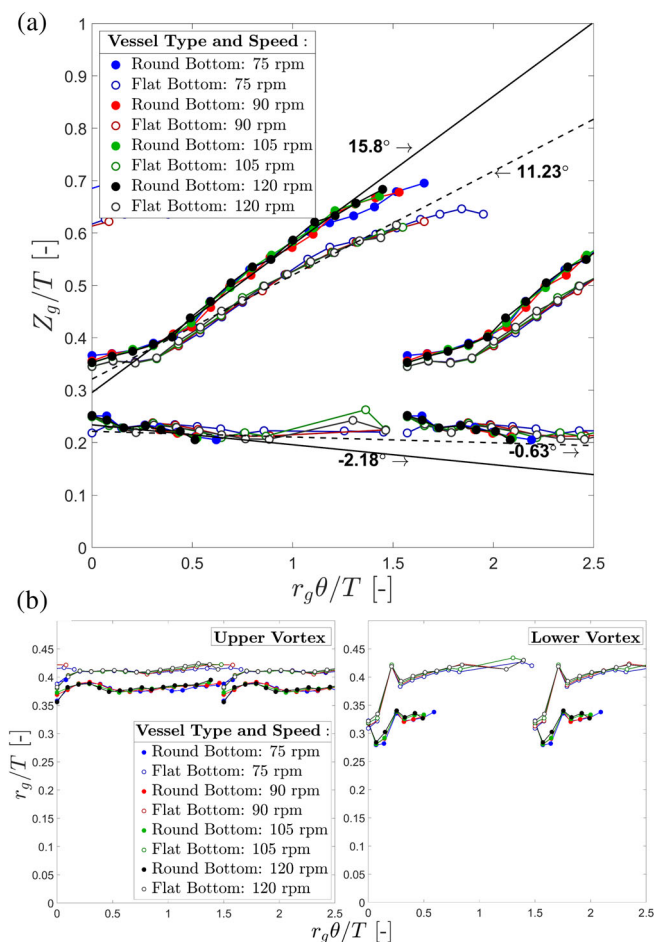
FIGURE 9 Trailing vortices characterization: (a) variation of the axial coordinate of the vortex center with increasing phase angle and (b) variation of the radial coordinate of the vortex center with increasing phase angle, upper vortex (left) and lower vortex (right) [Color figure can be viewed at wileyonlinelibrary.com]

FIGURE 10 Variation of the axial coordinate of the vortex center with increasing phase angle for the continuous (N = 90 rpm) and intermittent (N = 90 rpm, T_{inv} = 30 s, and T_{dwell} = 20,000 ms) agitation modes, directly after the stop in impeller motion [Color figure can be viewed at wileyonlinelibrary.com]

locus of the trailing vortices axes for a nondimensional azimuthal distance of $r_g\theta/T$ = 0–2.5 behind the leading blade for the axial coordinate of both vortices (a) and the radial coordinate (b). Estimates are provided for both bioreactor configurations at each rotational speed investigated (i.e., N = 75–120 rpm). The vortex axis is visualized in Figure 9a with a line fitted through the axial coordinate of the vortex center obtained for each phase angle. The line was fitted through all data points, with the exception of the first three, with an R^2 value ≥.98. It is evident that the trailing vortices axes are independent of the rotational speed. The inclination with respect to the horizontal plane of the upper vortex is higher (15.8°) for the round bottom bioreactor than for the flat bottom (11.2°); however, for the flat bottom configuration, the vortex intensity is more significant over a larger range of phase angles following the leading blade. The upper vortex is seen to decay below the defined vorticity threshold at $r_g\theta/T$ = 1.5–2 for the flat bottom tank, while for the round bottom this occurs at $r_g\theta/T$ = 1.4–1.7. The lower vortex is also shown to remain relatively horizontal throughout for both configurations.
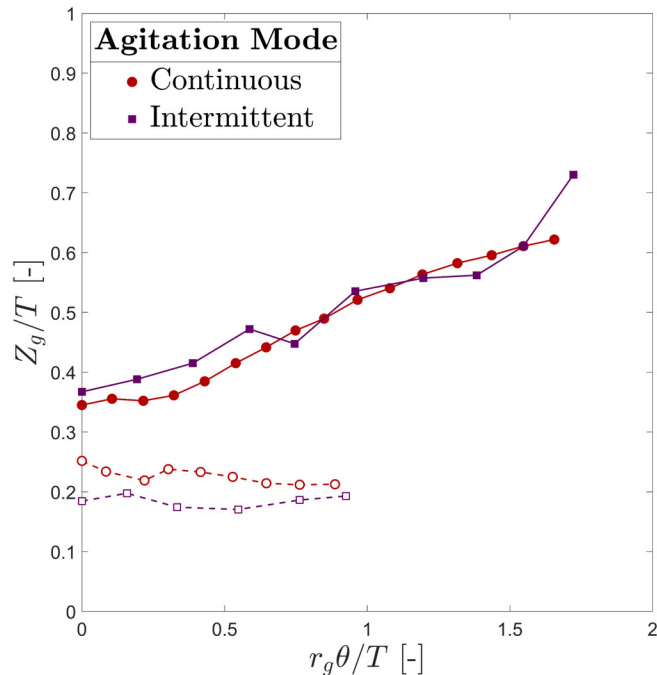
Observing the radial coordinate in both the upper and lower vortices, shown in Figure 9b, there is generally minimal radial displacement of the trailing vortices. This behavior is expected given the proximity of the bioreactor wall to the impeller blade tips and the axial nature of the impeller. Interestingly, the flat bottom configuration shows the trailing vortices to reside much closer to the bioreactor walls (i.e., r/T = 0.5) in comparison to the round configuration. A similar behavior is observed below the impeller, but this is mostly attributed to the change in geometry. For both configurations, the lower vortex exhibits radial coordinates closer to the reactor axis than their upper vortex counterpart (Figure 9b). This aspect is true for the flat bottom configuration only closer to the leading blade, while as the phase angle increases the vortex rapidly displaces toward the bioreactor wall.

Similar to what has been previously described for radial flow Rushton turbine impellers,[13-15] two counter rotating vortices are formed in the paddle impeller blade's wake, with the lower vortex showing little radial and axial displacement. The slight radial displacement and more significant axial displacement of the upper vortex are more comparable with that described in the literature for axial pitched blade turbine impellers.[18] Interestingly, Ismadi et al studied the flow dynamics of a spinner flask, commonly used in stem cell culture, also equipped with a radial flow paddle impeller with a large impeller to tank diameter ratio, D/T = 0.87, and found two counter rotating vortices formed in the impeller blade's wake, where the upper vortex also displays positive axial displacement. In addition, this study looked at

different impeller clearances and found the lower vortex became most dominant when the impeller clearance is highest and most similar to the configuration in this work with the flat-bottomed vessel.[42]

3.4 | Flow dynamics during intermittent agitation

The second part of this study sought to investigate the impact on the local flow of intermittent agitation modes within the flat bottom configuration. A range of dwell durations were investigated to observe the transient occurring before, during and after the dwell phase such as to quantify changes in flow dynamics. Similar to Figure 9a, the axial coordinate of the vortex center is plotted in Figure 10 for both the continuous (red) and intermittent (purple) agitation modes ($N = 90$ rpm). For the continuous agitation mode, the data reported in Figure 10 correspond to one impeller revolution ($\theta = 0–360°$) and were obtained with the phase-resolved analysis described in the previous section. For the intermittent agitation condition, the impeller is stationary, and therefore the tangential coordinate on the abscissa was estimated by multiplying the hypothetical rotational speed of the impeller, if it had kept rotating, and the time elapsed from the stoppage of the impeller. It is interesting to note the good agreement between the two plots, which suggests that despite the impeller stoppage the fluid carries enough inertia to maintain the local flow and vortex dynamics also for intermittent agitation. The vortex strength

decays only after the first revolution as vorticity goes below the selected threshold to determine its vortex center (Equation (1)).

To better observe the evolution of the flow during the transient in intermittent agitation modes, space averages were calculated according to Equation (2):

$$X^* = \frac{1}{A}\int_A X^* dA \tag{2}$$

where A is the measurement area and X^* represents either the velocity magnitude or the shear rate.

Figure 11 shows the space-averaged velocity magnitude, $\langle U_{rz}^* \rangle / V_{tip}$, considered over the entire vertical measurement plane for increasing durations of dwell time, $T_{dwell} = 500–30,000$ ms at $N = 90$ rpm and $T_{inv} = 30$ s. The plot shows the temporal changes in velocity magnitude over three distinct regions. The first region ($Nt = 5–45$) comprises an interval of continuous impeller rotation, represented in the first contour map below, considered hereafter as the "steady state." It is worth noting that the color bar for all contour maps is the same as that used in Figures 4 and 5. The second region, defined for $T_{dwell} = 20,000$ ms in Figure 11, represents the dwell phase and is initiated from $Nt = 45$, lasting for the duration of the dwell condition under investigation, followed by a successive interval of impeller rotation (Region 3). This represents a composition of two different sets of experiments. Regions 1 and 3 were measured during impeller
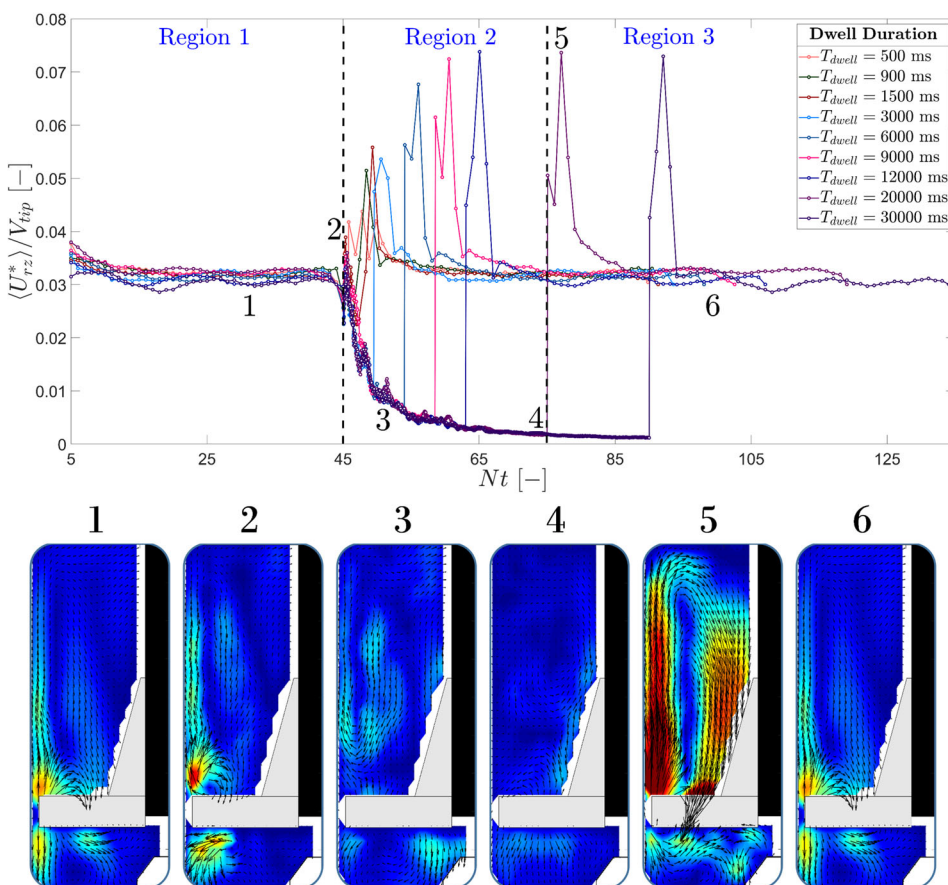

FIGURE 11 Space-averaged phase-resolved velocity magnitudes for intermittent agitation, $N = 90$ rpm, $T_{inv} = 30$ s, and $T_{dwell} = 500–30,000$ ms. Numbering on the plot indicates the contour maps of various timepoints throughout (1–6), visualized beneath [Color figure can be viewed at wileyonlinelibrary.com]

FIGURE 12 Space-averaged phase-resolved shear rate for intermittent agitation, N = 90 rpm, T_{inv} = 30 s, and T_{dwell} = 500–30,000 ms, separated according to the impeller region ($z/H_L \leq 0.45$) and bulk region ($z/H_L > 0.45$). Numbering on each plot indicates the contour maps of various timepoints throughout (1–6), visualized beneath [Color figure can be viewed at wileyonlinelibrary.com]
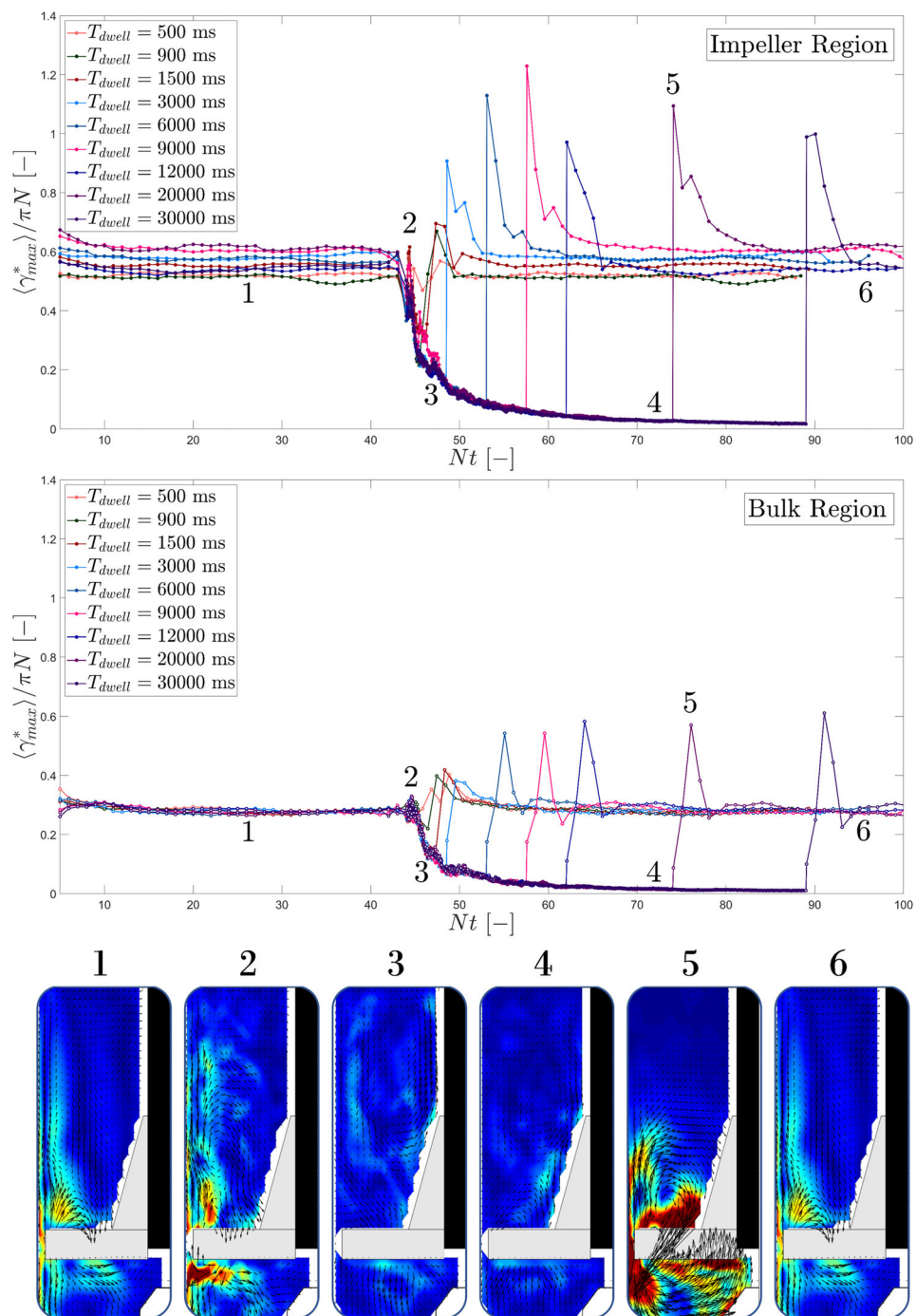
rotation and each data point corresponds to one impeller revolution, f = 1.5 Hz, when the impeller blade is in the plane of measurement (φ = 0°). Region 2 was measured in a second set of experiments, during the dwell. To fully capture the transient flow dynamics the frame rate was increased to f = 20 Hz.

Following the start of the dwell phase at Nt = 45 (Figure 11), a small spike in the space-averaged velocity magnitudes measured can be observed, an approximate increase of 7% from the determined "steady state." This spike lasts for approximately one revolution following the stop in impeller motion as shown by the second contour map at the bottom of Figure 11. The increase in velocity in

correspondence to the trailing vortices is due to the inertia carried by the bulk flow which hits the stationary impeller and gets deflected. Following this initial spike, the velocity magnitude is observed to rapidly decay (contour map #3) as the number of missed revolutions increases. A fully static flow is observed from approximately $T_{dwell} \geq$ 12,000 ms (contour map #4). With the restart of impeller motion, which is staggered and no longer shown to superimpose due to the varying durations of dwell time, a second more intense spike in velocity magnitude can be observed (contour map #5). The amplitude of the spike following the dwell is shown to linearly increase with T_{dwell} duration (between +35 and 138% the steady-state value). The

increasing spike is observed to plateau when a fully static system is reached, between T_{dwell} = 12,000–30,000 ms. It is apparent that the shorter dwell conditions maintain some degree of inertia in the flow. There is less acceleration as the flow is already moving; therefore, the highest amplification of the spike is observed when lower velocities or a static flow is present in the reactor before the restart in impeller rotation. After approximately four revolutions, this spike is shown to drop back to the steady state, representing continuous impeller rotation (contour map #6). It is worth noting that Nt = 0–5 are not shown due to the spike from the previous dwell phase.

Of great interest in cell culture applications is the shear forces imparted within a bioreactor, especially during intermittent agitation. To observe the overall impact of the transient between different dwell times, space-averaged results for shear rate, $\langle \gamma_{max}^* \rangle / \pi N$, are presented in Figure 12. In this case, the space averages were carried over two different areas: the impeller region ($z/H_L \leq 0.45$) and the bulk region ($z/H_L > 0.45$). As before, Figure 12 shows a nearly constant "steady-state" nondimensional shear rate, occurring during continuous impeller rotation (contour map #1, $\langle \gamma_{max} \rangle / \pi N$ = 0–0.12) before a small spike is observed with the start of the dwell phase (contour map #2). Rapid decay in the shear rate is observed (contour map #3) with the increased number of missed revolutions until the flow is considered fully static and the shear rate is negligible (contour map #4). It is interesting to observe the similar profiles between the impeller and bulk regions, with higher shear rates overall within the impeller region. The initial spike with the stop in impeller motion (contour map #2) is slightly more prominent in the bulk region (+5% the steady-state shear value) and a second more intense spike is again observed during the transient with the restart in impeller motion (contour map #5). It is now interesting to observe for longer dwell durations ($T_{dwell} \geq 12,000$ ms) the space-averaged shear rate considered in the impeller region reduces in intensity and does not plateau, as previously seen in Figure 11. This is due to the fully static flow before the impeller restart resulting in a more intense circulation loop, which is distributed across the whole plane. Observing the bulk region in Figure 12, a small delay from the impeller restart to the peak space-averaged shear rate can be observed as the recirculation loop starts to reform. The transient spike for both regions is shown to resume the steady state following approximately four revolutions (contour map #6). When considering across the whole plane of measurement, the space-averaged shear rate shows the same linear increase with increasing T_{dwell} duration (+20–81.6% the respective steady-state value) until a plateau is reached for $T_{dwell} \geq 12,000$ ms, when the flow is considered fully static before the restart in impeller motion. The highest achieved local shear rate, $\langle \gamma_{max} \rangle / \pi N$ = 4.67, measured from phase-resolved data during the more intense spike following the dwell phase, is equivalent to dimensional shear stresses of τ = 0.022 Pa. This is an approximate 78% increase to the maximum measured shear during continuous agitation, however, remains fivefold lower than values reported in literature to impair stem cell proliferation and viability.[26] Ismadi et al investigated the flow dynamics within a spinner flask equipped with a paddle impeller with a large impeller to tank diameter ratio (D/T = 0.87), and

characterized shear stress levels comparable to those found in this work.[42] Due to the extremely sensitive nature of stem cells, although the levels of shear are not predicted to detrimentally impact upon cell proliferation, the varying levels of shear within the flow is most likely to be a contributing factor to the commitment of differentiation pathways, and could explain the increase in cell differentiation yields of iPSCs obtained by Samaras et al[2] for increasing dwell durations, T_{dwell} = 500–1,500 ms.

4 | CONCLUSIONS

This work showed the bioreactor configuration can have a significant impact upon the flow dynamics, which in turn may impact upon a number of other factors including the biological outcomes. The rigorous characterization of both bioreactor types is novel to the field and can be used to inform upon future studies utilizing the two configurations investigated.

Correia et al[1] performed the same iPSC differentiation experiments in the two DASGIP configurations investigated in this work and found differentiation yields were most favorable when culture was performed within the flat bottom configuration in comparison to the torispherical, rounded bottom configuration of the DASGIP. Understanding the flow occurring in each bioreactor configuration helps to elucidate why a particular configuration is favorable.

Flow dynamics for the flat and round bottom DASGIP bioreactor systems with a change in impeller clearance, were characterized to assess differences in flow pattern and vorticity. Both bioreactor configurations proved to scale well across a range of rotational speeds and showed the paddle impeller equipped to generate two trailing vortices; the upper vortex is shown to exhibit a high inclination, traveling up the bioreactor wall in the impeller blades' wake, while the lower vortex is shown to change in intensity with the bottom geometry and impeller clearance. The flat bottom configuration showed two equal counter-rotating trailing vortices, while the round configuration exhibited a weaker trailing vortex below the impeller. The more intense lower vortex in the flat bottom configuration, which persisted for almost a full impeller rotation, is anticipated to generate a region of improved mixing and suspension of cell aggregates below the impeller, thus resulting in an improvement of cell culture.

The two-blade paddle impeller configuration had a very high D/T which resulted in a reduction of the axial and radial velocity components, however this also created extremely low shear stresses in the regions of highest anticipated shear. Based upon the vorticity and velocity magnitudes, it was observed that the paddle impeller configuration exhibited flow characteristics most comparable to an axial flow impeller.

The application of intermittent agitation showed significant changes to the flow profiles characterized. Close observation of the flow at the beginning of the dwell phase showed a small transient spike in velocity magnitude and shear rate before the flow parameters were observed to decay until approximately T_{dwell} = 12 s, when the flow was estimated to become fully stationary. Based upon space-averaged results considering a central vertical plane through the

impeller, a small transient impulse (+7 and +5% the considered steady state) in velocity magnitude and shear rate at the incidence of the dwell phase was observed. A second, more intense spike was observed with the restart in impeller motion, the magnitude of which was shown to linearly increase with the dwell duration, until longer dwell times where a static flow was reached at the end of the dwell ($T_{\text{dwell}} \geq 12,000$ ms), and the observed spike was shown to plateau. The maximum amplification in the transient after the dwell reached up to 138 and 82%, respectively for velocity magnitude and shear. The highest shear stresses determined during intermittent agitation remained fivefold lower than those in literature deemed detrimental to iPSC cell proliferation.[26]

ACKNOWLEDGMENTS

ORCID

Jasmin J. Samaras https://orcid.org/0000-0001-5668-4569
Martina Micheletti https://orcid.org/0000-0001-5147-0182
Andrea Ducci https://orcid.org/0000-0003-0198-9634

REFERENCES

1. Correia C, Serra M, Espinha N, et al. Combining hypoxia and bioreactor hydrodynamics boosts induced pluripotent stem cell differentiation towards cardiomyocytes. *Stem Cell Rev*. 2014;10(6):786-801. https://doi.org/10.1007/s12015-014-9533-0.
2. Samaras JJ, Abecasis B, Serra M, Ducci A, Micheletti M. Impact of hydrodynamics on iPSC-derived cardiomyocyte differentiation processes. *J Biotechnol*. 2018;287:18-27. https://doi.org/10.1016/j.jbiotec.2018.07.028.
3. Kwok CK, Günther K, Ergün S, Heron A, Edenhofer F, Rook M. Scalable stirred suspension culture for the generation of billions of human induced pluripotent stem cells using single-use bioreactors. *Journal of Tissue Engineering and Regenerative Medicine*. 2017;2018:1076-1087. https://doi.org/10.1002/term.2435.
4. Kropp C, Kempf H, Halloin C, et al. Impact of feeding strategies on the scalable expansion of human pluripotent stem cells in single-use stirred tank bioreactors. *Stem Cells Transl Med*. 2016;5(10):1289-1301. https://doi.org/10.5966/sctm.2015-0253.
5. van Eikenhorst G, Thomassen YE, van der Pol LA, Bakker WAM. Assessment of mass transfer and mixing in rigid lab-scale disposable bioreactors at low power input levels. *Biotechnol Prog*. 2014;30(6):1269-1276. https://doi.org/10.1002/btpr.1981.
6. Olmer R, Lange A, Selzer S, et al. Suspension culture of human pluripotent stem cells in controlled, stirred bioreactors. *Tissue Eng Part C Methods*. 2012;18(10):772-784. https://doi.org/10.1089/ten.tec.2011.0717.
7. Rutherford K, Lee KC, Mahmoudi SMS, Yianneskis M. Hydrodynamic characteristics of dual rushton impeller stirred vessels. *AIChE J*. 1996;42(2):332-346. https://doi.org/10.1002/aic.690420204.
8. Escudie R, Line A. Experimental analysis of hydrodynamics in a radially agitated tank. *AIChE J*. 2003;49(3):585-603.
9. Doulgerakis Z, Yianneskis M, Ducci A. On the interaction of trailing and macro-instability vortices in a stirred vessel-enhanced energy levels and improved mixing potential. *Chem Eng Res Des*. 2009;87(4):412-420. https://doi.org/10.1016/j.cherd.2008.12.019.
10. Yianneskis M, Popiolek Z, Whitelaw JH. An experimental study of the steady and unsteady flow characteristics of stirred reactors. *J Fluid Mech*. 1987;175:537-555. https://doi.org/10.1017/S002211208700051X.
11. Costes J, Couderc JP. Study by laser Doppler anemometry of the turbulent flow induced by a Rushton turbine in a stirred tank: influence of the size of the units—II. Spectral analysis and scales of turbulence. *Chem Eng Sci*. 1988;43(10):2765-2772. https://doi.org/10.1016/0009-2509(88)80019-8.
12. Stoots CM, Calabrese RV. Mean velocity field relative to a Rushton turbine blade. *AIChE J*. 1995;41(1):1-11. https://doi.org/10.1002/aic.690410102.
13. Delafosse A, Morchain J, Guiraud P, Liné A. Trailing vortices generated by a Rushton turbine: assessment of URANS and large Eddy simulations. *Chem Eng Res Des*. 2009;87(4):401-411. https://doi.org/10.1016/j.cherd.2008.12.018.
14. Escudié R, Bouyer D, Liné A. Characterization of trailing vortices generated by a Rushton turbine. *AIChE J*. 2004;50(1):75-86. https://doi.org/10.1002/aic.10007.
15. Van't Riet K, Smith JM. The trailing vortex system produced by Rushton turbine agitators. *Chem Eng Sci*. 1975;30(9):1093-1105. https://doi.org/10.1016/0009-2509(75)87012-6.
16. Armstrong SG, Ruszkowsk S. Measurement and comparison of flows generated by different types of impeller in a stirred tank. Proceedings of the Colloquium on Mechanical Agitation. Toulouse; 1987:1.9–1.16.
17. Hockey RM, Nouri JM. Turbulent flow in a baffled vessel stirred by a 60° pitched blade impeller. *Chem Eng Sci*. 1996;51(19):4405-4421. https://doi.org/10.1016/0009-2509(96)00267-9.
18. Schäfer M, Yianneskis M, Wächter P, Durst F. Trailing vortices around a 45° pitched-blade impeller. *AIChE J*. 1998;44(6):1233-1246. https://doi.org/10.1002/aic.690440602.
19. Ramsay J, Simmons MJH, Ingram A, Stitt EH. Mixing of Newtonian and viscoelastic fluids using "butterfly" impellers. *Chem Eng Sci*. 2016;139:125-141. https://doi.org/10.1016/j.ces.2015.09.026.
20. Hall JF, Barigou M, Simmons MJH, Stitt EH. Comparative study of different mixing strategies in small high throughput experimentation reactors. *Chem Eng Sci*. 2005;60:2355-2368. https://doi.org/10.1016/j.ces.2004.10.045.
21. Hall JF, Barigou M, Simmons MJH, Stitt EH. Mixing in unbaffled high-throughput experimentation reactors. *Ind Eng Chem Res*. 2004;43(15):4149-4158. https://doi.org/10.1021/ie049872q.
22. Montante G, Bakker A, Paglianti A, Magelli F. Effect of the shaft eccentricity on the hydrodynamics of unbaffled stirred tanks. *Chem Eng Sci*. 2006;61(9):2807-2814. https://doi.org/10.1016/j.ces.2005.09.021.
23. Tamburini A, Gagliano G, Micale G, Brucato A, Scargiali F, Ciofalo M. Direct numerical simulations of creeping to early turbulent flow in unbaffled and baffled stirred tanks. *Chem Eng Sci*. 2018;192:161-175. https://doi.org/10.1016/j.ces.2018.07.023.
24. Yoshida M, Ebina H, Shirosaki H, Ishioka K, Oiso K. Liquid flow in impeller swept regions of baffled and unbaffled vessels with a turbine-type agitator. *Brazilian J Chem Eng*. 2015;32(4):865-873. https://doi.org/10.1590/0104-6632.20150324s00003682.
25. Ciofalo M, Brucato A, Grisafi F, Torraca N. Turbulent flow in closed and free-surface unbaffled tanks stirred by radial impellers. *Chem Eng Sci*. 1996;51(14):3557-3573.
26. Ismadi M, Gupta P, Fouras A, et al. Flow characterization of a spinner flask for induced pluripotent stem cell culture application. *PLoS One*. 2014;9(10):1-11. https://doi.org/10.1371/journal.pone.0106493.

27. Wang W, Ha CH, Jhun BS, Wong C, Jain MK, Jin Z. Fluid shear stress stimulates phosphorylation-dependent nuclear export of HDAC5 and mediates expression of KLF2 and eNOS. *Blood*. 2010; 115(14):2971-2980. https://doi.org/10.1182/blood-2009-05-224824.

28. Huang Y, Zheng L, Gong X, et al. Effect of cyclic strain on cardiomyogenic differentiation of rat bone marrow derived mesenchymal stem cells. *PLoS One*. 2012;7(4):e34960. https://doi.org/10.1371/journal.pone.0034960.

29. Tannaz NA, Ali SM, Nooshin H, et al. Comparing the effect of uniaxial cyclic mechanical stimulation and chemical factors on myogenin and Myh2 expression in mouse embryonic and bone marrow derived mesenchymal stem cells. *Mol Cell Biomech*. 2014;11(1):19-37.

30. Sumanasinghe RD, Bernacki SH, Loboa EG. Osteogenic differentiation of human mesenchymal stem cells in collagen matrices: effect of uniaxial cyclic tensile strain on bone morphogenetic protein (BMP-2) mRNA expression. *Tissue Eng*. 2006;12(12):3459-3465. https://doi.org/10.1089/ten.2006.12.3459.

31. Liu S, Ruban L, Wang Y, Zhou Y, Nesbeth DN. Establishing elements of a synthetic biology platform for Vaccinia virus production: Bio-Brick™ design, serum-free virus production and microcarrier-based cultivation of CV-1 cells. *Heliyon*. 2017;3(2):e00238. https://doi.org/10.1016/j.heliyon.2017.e00238.

32. Fernandes AM, Marinho PAN, Sartore RC, et al. Successful scale-up of human embryonic stem cell production in a stirred microcarrier culture system. *Brazilian J Med Biol Res*. 2009;42(6):515-522. https://doi.org/10.1590/s0100-879x2009000600007.

33. Dos Santos F, Andrade PZ, Eibes G, da Silva CL, Cabral JMS. Ex vivo expansion of human mesenchymal stem cells on microcarriers. *Methods Mol Biol*. 2011;698:189-198. https://doi.org/10.1007/978-1-60761-999-4_15.

34. Nienow AW, Hewitt CJ, Heathman TRJ, et al. Agitation conditions for the culture and detachment of hMSCs from microcarriers in multiple bioreactor platforms. *Biochem Eng J*. 2016;108:24-29. https://doi.org/10.1016/j.bej.2015.08.003.

35. Samaras JJ, Ducci A, Micheletti M. Suspension and mixing characterization of intermittent agitation modes in DASGIP bioreactors. *Chem Eng Technol*. 2019;42(00):1-8. https://doi.org/10.1002/ceat.201900069.

36. Ducci A, Weheliye W. Orbitally shaken bioreactor—viscosity effects on flow characteristics. *AIChE J*. 2014;60(11):3951-3968. https://doi.org/10.1002/aic.

37. Bouremel Y, Yianneskis M, Ducci A. On the utilisation of vorticity and strain dynamics for improved analysis of stirred processes. *Chem Eng Res Des*. 2009;87(4):377-385. https://doi.org/10.1016/j.cherd.2008.11.016.

38. Baldi S, Yianneskis M. On the direct measurement of turbulence energy dissipation in stirred vessels with PIV. *Ind Eng Chem Res*. 2003;42(26):7006-7016. https://doi.org/10.1021/ie0208265.

39. Odeleye AOO, Marsh DTJ, Osborne MD, Lye GJ, Micheletti M. On the fluid dynamics of a laboratory scale single-use stirred bioreactor. *Chem Eng Sci*. 2014;111:299-312. https://doi.org/10.1016/j.ces.2014.02.032.

40. Aubin J, le Sauze N, Bertrand J, Fletcher DF, Xuereb C. PIV measurements of flow in an aerated tank stirred by a down- and an up-pumping axial flow impeller. *Exp Therm Fluid Sci*. 2004;28(5):447-456. https://doi.org/10.1016/j.expthermflusci.2001.12.001.

41. Wu H, Patterson GK. Laser Doppler measurements of turbulent flow parameters in a stirred mixer. *Chem Eng Sci*. 1989;44(10):2207-2221.

42. Ismadi M, Hourigan K, Fouras A. Experimental characterization of fluid mechanics in a spinner flask bioreactor. *Processes*. 2014;2(4): 753-772. https://doi.org/10.3390/pr2040753.